

Article

A Distributed Terahertz Metasurface with Cold-Electron Bolometers for Cosmology Missions

Behrokh Beiranvand ^{1,*}, Alexander S. Sobolev ^{1,2}, Michael Yu. Larionov ¹ and Leonid S. Kuzmin ^{3,4}

¹ Moscow Institute of Physics and Technology, National Research University, 9 Institutskiy per., Dolgoprudny, 141701 Moscow, Russia; sobolev@hitech.cplire.ru (A.S.S.); mikhaillarionov@phystech.edu (M.Y.L.)

² Kotelnikov Institute of Radio Engineering and Electronics RAS, Mokhovaya st. 11/7, 125009 Moscow, Russia

³ Department of Microtechnology and Nanoscience, Chalmers University of Technology, SE-412 96 Gothenburg, Sweden; kuzmin@chalmers.se

⁴ Nizhny Novgorod State Technical University n.a. R.E. Alekseev, GSP-41, 603950 Nizhny Novgorod, Russia

* Correspondence: beiranvand@phystech.edu or eng.beiranvand@gmail.com

Abstract: We developed and tested a 2D periodic array of cold-electron bolometers arranged into a wideband frequency selective metasurface that absorbs more than 70% of the incident power in the frequency range 100–800 GHz. The array had 10×10 unit cells, each containing four bolometers incorporated into a ring. The chip with bolometers was mounted on the back side of the silicon lens without a back-reflector. Preliminary experiments demonstrated voltage responsivity as high as 10^9 V/W for the current-biased series array. Simulation of the noise performance shows realization of background noise-limited performance with $NEP_{tot} < NEP_{phot}$ for the optical power load $P_0 > 15$ pW. Results of numerical simulation made for the unit cell of the array are presented together with the equivalent diagram based on lumped network elements. The unit cell also was developed numerically to operate in two radiation modes.

Keywords: cold-electron bolometer; frequency selective metasurface; terahertz detector; cryogenic device



Citation: Beiranvand, B.; Sobolev, A.S.; Larionov, M.Y.; Kuzmin, L.S. A Distributed Terahertz Metasurface with Cold-Electron Bolometers for Cosmology Missions. *Appl. Sci.* **2021**, *11*, 4459. <https://doi.org/10.3390/app11104459>

Academic Editor: Antonio Di Bartolomeo

Received: 9 April 2021

Accepted: 11 May 2021

Published: 14 May 2021

Publisher's Note: MDPI stays neutral with regard to jurisdictional claims in published maps and institutional affiliations.



Copyright: © 2021 by the authors. Licensee MDPI, Basel, Switzerland. This article is an open access article distributed under the terms and conditions of the Creative Commons Attribution (CC BY) license (<https://creativecommons.org/licenses/by/4.0/>).

1. Introduction

A cold-electron bolometer (CEB) is a cryogenic device with a tiny absorbing normal metal stripe connected to the two superconducting electrodes via superconductor–insulator–normal metal (SIN) tunnel junctions [1,2]. The incoming RF-signal increases the temperature of electrons in the normal metal, however in the presence of DC current hot electrons leave the absorber via SIN-junctions. An effect of electron cooling by the bias current increases the dynamic range of CEBs and reduces their noise equivalent power (NEP) [3–5]. Currently, the NEP level of CEBs is shown to be close to the photon noise limit [6,7], which makes CEBs attractive for balloon-borne radio astronomical missions such as the Large Scale Polarization explorer (LSPE) [8] and OLIMPO [9]. When CEBs are arranged into a periodic 2D array acting as a frequency selective surface (FSS) the incident RF signal is evenly distributed between all the bolometers. The resulting saturation RF-power of the array pixel is higher than that of a single bolometer by the factor which approximately equals the number of bolometers in the pixel. For achieving optimal NEP with reasonably high responsivity, the low-frequency impedance of the array should be matched to the impedance of the readout amplifiers. This can be done by an appropriate combination of parallel and series DC-connections between elementary unit cells [10]. It was shown in [11–13] that bolometric arrays consisting of the half-wavelength unit cells and fabricated on thick substrates provided 5–10% bandwidth. A reasonable agreement was obtained [12,13] between the experimentally measured frequency response and the one numerically calculated for the unit cell. In this paper we present the concept of an ultra-wideband array of CEBs with the unit cell size of the order of $\lambda/10$ at the central frequency 350 GHz.

2. Numerical Model

The effective surface impedance Z_{FSS} (Ohm per square) of the periodic array of CEBs should be matched to the electrodynamic environment. Unlike conventional frequency selective surfaces, which do not contain active elements, a layout of the unit cell of the bolometric array must contain DC-lines for biasing and readout. It turns out that the way how DC-biasing issue is resolved determines the polarization of the incoming signal the array is sensitive to. The equivalent diagram of the array sitting on the back of a silicon lens without a back-reflector can be represented (see Figure 1) by the two impedances, vacuum impedance (Z_{VAC}) and silicon impedance (Z_{SI}) connected in parallel to Z_{FSS} . They are frequency independent and correspond to the characteristic impedances of the vacuum and the silicon half-spaces. If $Z_{FSS} = 90 \Omega$ then P_{abs} , the fraction of the RF-power coupled from Z_{SI} to Z_{FSS} , will be about 80% [14].

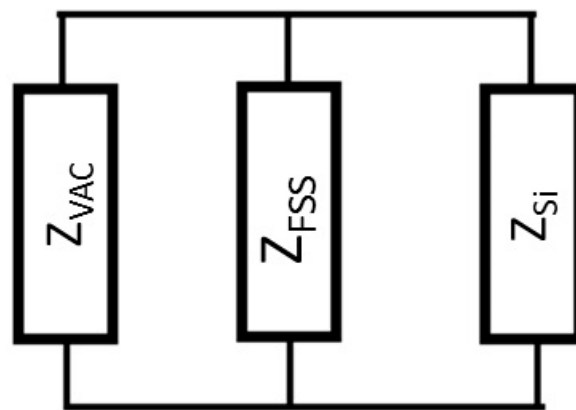


Figure 1. Equivalent diagram.

Figure 2 shows the model of the unit cell with dimensions $64 \mu\text{m} \times 64 \mu\text{m}$ in XY-plane and its SEM image. The array is designed for receiving linear Y-polarized signal corresponding to the Floquet mode #1 and coming from the silicon half-space. E-field of the mode#1 is parallel to the DC-biasing lines that provide Z_{FSS} close to the optimal value 90Ω in a wide frequency range. Gaps between the neighboring rings result in capacitive Z_{FSS} and therefore poor matching with Z_{SI} . The orthogonal mode #2 is sensitive to the gaps between the neighboring rings and has poor matching because of capacitive Z_{FSS} . The unit cell has periodic boundaries in X and Y directions, while the two Floquet ports are defined at the boundaries corresponding to the maximum and the minimum of z-coordinates. These parts are touching vacuum and silicon spaces correspondingly. The reference planes of both ports are touching the array of model by a lumped element with a series connection of resistance R and capacitance C . For a real CEB, R is determined by the DC resistance of the normal absorber, while C is the capacitance of the two SIN-junctions connected in series to the absorber. The optimal capacitance $C = 20 \text{ fF}$ and the resistance $R = 100 \Omega$ for each CEB.

Small unit cell size allows for absorption by the bolometric array in a wide range of both frequency and incidence angle φ . The dependence of P_{abs} as a function of frequency and φ computed for the two orthogonal modes is shown in Figure 3. In these simulations φ is defined in YZ-plane. The focus of a silicon lens is a waist of the Gaussian beam, where the condition of the planar normally incident wave is nearly satisfied. For normal incidence the array absorbs nearly 80% of mode#1 power in the range from 100 GHz to 800 GHz. However, Figure 3a demonstrates moderate P_{abs} for φ values up to 40 degrees. This fact makes the array promising for integration into a waveguide or a back-to-back horn, where the k-vector of the incident wave has tangential component to the plane of the absorbing array.

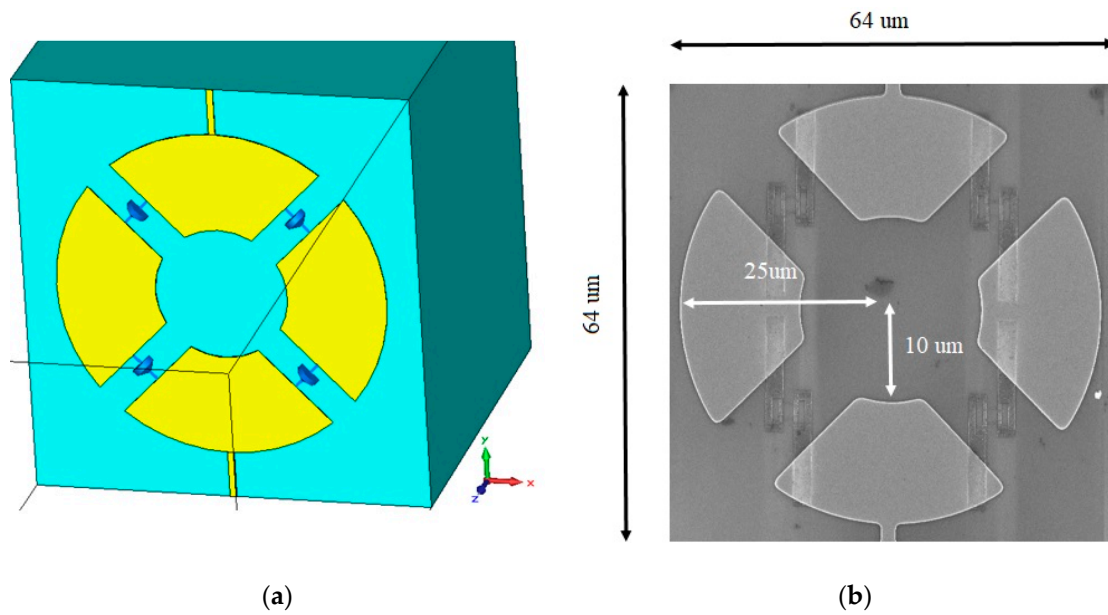


Figure 2. Unit cell of the CEB array: (a) 3D model with lumped elements representing CEBs [14], (b) SEM-image.

With a new modification of the unit cell (see numerical model shown in Figure 4a) the array of CEBs absorbs an acceptable amount of power from two orthogonal modes. The equivalent network of a single ring with the four bolometers can be represented by that of a single bolometer and the inductance of the ring Lr excited by a plane wave (see Figure 4b). Capacitive coupling between the adjacent rings in the array is associated with capacitance Cr , which creates negative contribution to the imaginary part of Z_{FSS} . Biasing wires between the rings can be represented by small resistance r connected in series with inductance Lw . Vertical wires seen by mode #1 have ohmic contacts to the rings, while horizontal wires seen by mode #2 with horizontal polarization have a thin SiO_2 layer between the wire pad and the ring in the overlapping area that creates series capacitance Cw , such that $Cw \gg Cr$. Impedance of wire inductance Lw is shunting large impedance of Cr and reduces its reactance to the value comparable to the reactance of the ring with the four CEBs. Both equivalent networks shown in Figure 4b and representing Z_{FSS} are equivalent to a series resonant network, which impedance around the resonant frequency is real and equal to the resistance $R = 100 \Omega$ of the CEB.

Figure 5 indicates calculated Z_{FSS} for both modes. As is shown, both modes can see the DC-biasing wires (the horizontal and vertical wires) and capacitive coupling between two adjacent unit cells can be tuned out at around 350 GHz for mode#1 and 750 GHz for mode#2. Series capacitance Cw shifts the absorption frequency for mode#2 and increases the absorption bandwidth (see Figure 6). Figure 6a shows absorption of the waves coming from the silicon half-space for both orthogonal modes, Absorption of arbitrary polarization $Pabs$ can be calculated as total absorption of different waves with amplitude a and random uniform distribution of polarization angle θ . The inset in Figure 6b shows vectors P1 and P2 corresponding to polarizations of mode #1 and mode #2. $Pabs$ can be found by taking a simple integral:

$$Pabs = \frac{Pabs^{(1)} + Pabs^{(2)}}{2} = |a|_2 \int_0^{\pi/2} \cos^2 \theta d\theta + |a|_2 \int_0^{\pi/2} \sin^2 \theta d\theta \quad (1)$$

where $Pabs^{(1)}$ is absorbed power of mode#1 and $Pabs^{(2)}$ is absorbed power of mode#2.

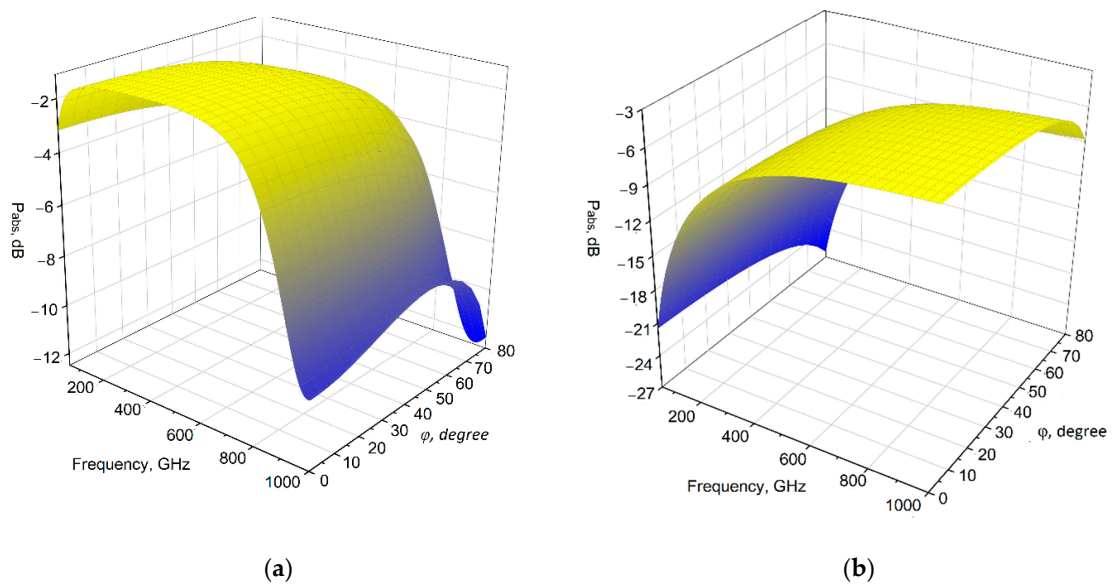


Figure 3. Computed P_{abs} for the FSS unit cell: (a) mode #1, (b) mode #2.

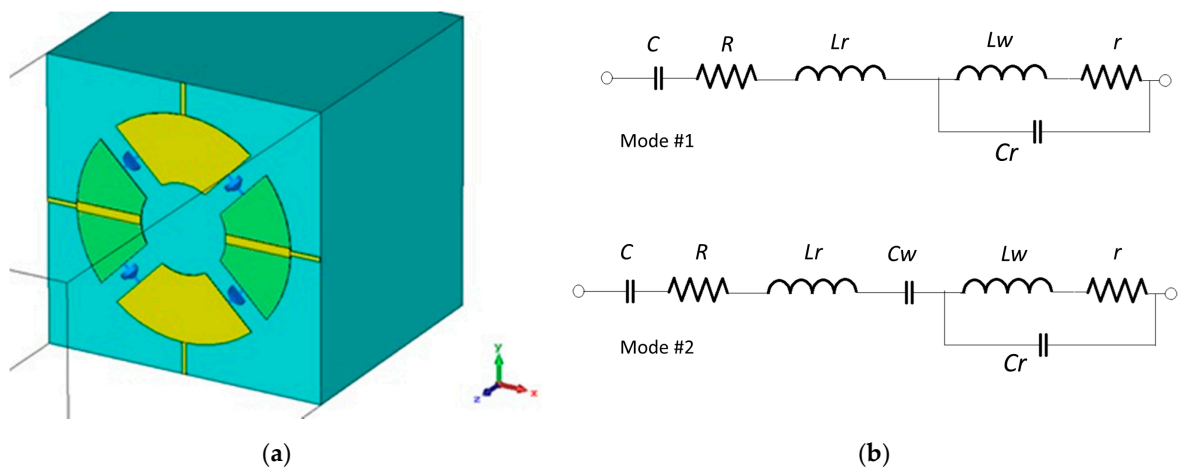


Figure 4. (a) Unit cell layout for dual mode sensing. (b) Equivalent circuits for Z_{FSS} for two orthogonal modes of the Floquet port.

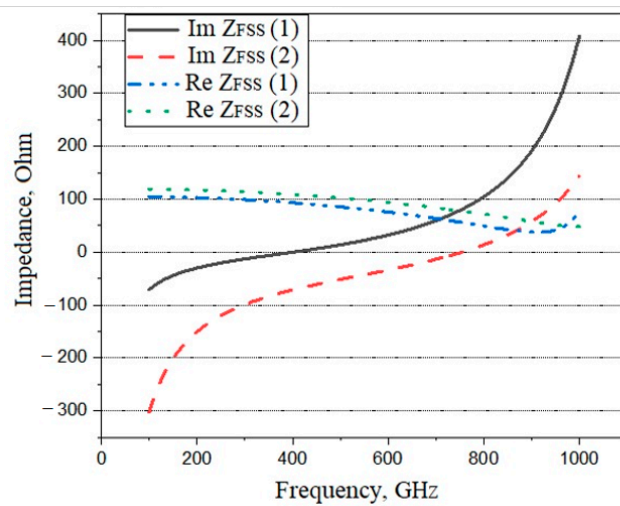


Figure 5. Real and imaginary impedances of Z_{FSS} calculated for mode#1 and mode#2.

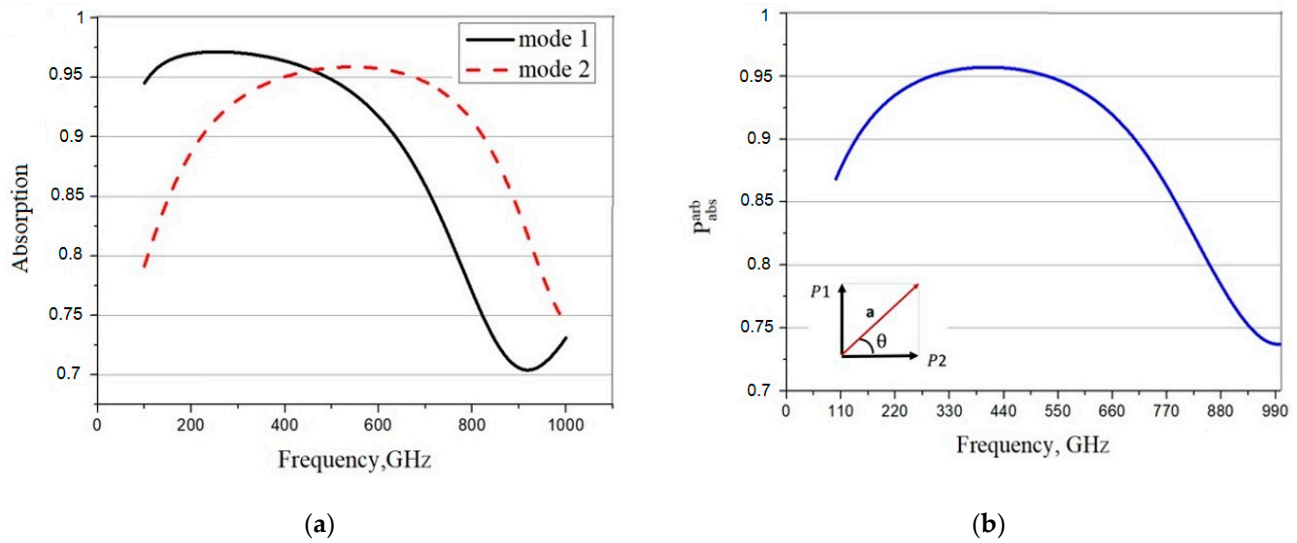


Figure 6. (a) P_{abs} of mode#1 and mode#2, (b) P_{abs}^{arb} of the unit cell for arbitrary polarization.

From Equation (1) the calculated absorbed power of both modes for the pattern of array with the optimized unit cell design as functions of frequency are provided and shown in Figure 6, which illustrates the results of a wideband of frequency range from 100 GHz to 1000 GHz. Figure 6a shows absorption for each mode separately and it can be seen for two modes the absorption is from 70% to more than 95%. According to Equation (1) the absorption power of the two modes can be concluded (see Figure 6b), which shows absorption more than 75% (from 75% to 95%).

3. Noise Analysis

In our noise analysis of the 2D CEB array we use the basic CEB model with a strong electrothermal feedback due to electron cooling [15,16] and the concept of series arrays in a current-biased mode [9]. The operation of a CEB array can be analyzed using the heat balance equation for a single CEB, taking into account the power distribution between the $N \times W$ bolometers:

$$P_{cool}(V, T_e, T_{ph}) + \Sigma \Lambda (T_e^5 - T_{ph}^5) + \frac{V^2}{R_j} + I^2 R_a = [P_0 + \delta P(t)]/W/N \quad (2)$$

Here, $\Sigma \Lambda (T_e^5 - T_{ph}^5)$ is the heat flow from the electron to the phonon subsystems in the absorber, Σ is a material constant, Λ is the volume of the absorber, T_e and T_{ph} are, respectively, the electron and phonon temperatures of the absorber, $P_{cool}(V, T_e, T_{ph})$ is the cooling power of the SIN tunnel junction, R_j is the sub-gap resistance of the tunnel junction, R_a is the resistance of the absorber, $\delta P(t)$ is the incoming RF power changes and P_0 is absorbed signal power. We can separate Equation (2) into the time independent term,

$$P_{SIN0}(V, T_{e0}, T_{ph}) + \Sigma \Lambda (T_{e0}^5 - T_{ph}^5) = P_0/W/N \quad (3)$$

and the time dependent term,

$$(\partial P_{SIN}/\partial T + 5\Sigma \Lambda T_e^4) \delta T = \delta P_1 \quad (4)$$

The first term in Equation (4), $G_{SIN} = \partial P_{SIN}/\partial T$, is the cooling thermal conductance of the SIN junction that gives the negative electrothermal feedback (ETF); when this term is large, it reduces the temperature response, δT , because the cooling power, P_{SIN} , compensates for the change of signal power in the bolometer. The second term in Equation (4), $G_{e-ph} = 5\Sigma \Lambda T_e^4$, is the electron-phonon thermal conductance of the absorber.

From Equation (4), we can define an effective complex thermal conductance that controls the temperature response of the CEB to the incident signal power:

$$G_{eff} = G_{SIN} + G_{e-ph} \quad (5)$$

In analogy with TES [10], the effective thermal conductance of the CEB is increased by electron cooling (negative ETF). Here, we assume that the *SIN* tunnel junctions are current-biased, and the voltage is measured by a JFET amplifier. The responsivity, S_V , is described by the voltage response to the incoming power:

$$S_V = \frac{\delta V_\omega}{\delta P_\omega} = \frac{\partial V / \partial T}{G_{e-ph} + G_{SIN}} \quad (6)$$

In the second term of Equation (7),

$$G_{SIN} = \frac{\partial P_{SIN}}{\partial T} - \frac{\partial P_{SIN}}{\partial V} \left(\frac{\partial I}{\partial T} / \frac{\partial I}{\partial V} \right) \quad (7)$$

is the cooling thermal conductance of the *SIN* junction, which provides some electron cooling and helps to avoid the overheating of the absorber.

Noise properties are characterised by the noise equivalent power (*NEP*), which is the sum of three contributions:

$$NEP_{tot}^2 = N * W * NEP_{e-ph}^2 + N * W * NEP_{SIN}^2 + NEP_{AMP}^2 \quad (8)$$

here, NEP_{e-ph} is the noise associated with electron–phonon interaction:

$$NEP_{e-ph}^2 = 10k_B \Sigma \Lambda (T_e^6 + T_{ph}^6) \quad (9)$$

In Equation (8), NEP_{SIN} is the noise of the *SIN* tunnel junctions. The *SIN* noise has three components: the shot noise, $2eI / S2I$, the fluctuation of the heat flow through the tunnel junctions, and the correlation between these two processes:

$$NEP_{SIN}^2 = \frac{\delta I_\omega^2}{(\frac{\partial I}{\partial V} S_V)^2} + 2 \frac{\langle \delta P_\omega \delta I_\omega \rangle}{\frac{\partial I}{\partial V} S_V} + \partial P_\omega^2 \quad (10)$$

Due to this correlation, the shot noise is increased by 30–50% in contrast to a CEB in voltage-biased mode, where strong anti-correlation decreases the shot noise.

The last term of Equation (8) depends on the voltage δV and the current δI noise of a JFET, which are expressed in $\text{nV Hz}^{-1/2}$ and $\text{pA Hz}^{-1/2}$:

$$NEP_{AMP}^2 = (\delta V^2 + (\delta I * (Rd + Ra) / W * N)^2) / (S_V / W)^2 \quad (11)$$

Estimations were made for the 150 GHz channel of balloon telescope LSPE.

The results of the simulation of the 2D array with JFET readout are shown in Figure 7.

Figure 7a shows realization of improved noise properties with total CEB noise $NEP_{tot} = 7 \times 10^{-17} \text{ W/Hz}^{1/2}$ less than photon noise of the signal $NEP_{phot} = 1.1 \times 10^{-16} \text{ W/Hz}^{1/2}$ for the array with a series and parallel combination of CEBs at the optical power load of 20 pW. Improvement of the NEP in 2D array is achieved due to distribution of the optical power load between 400 CEBs and the decrease in the amplifier noise, as determined by the product of the amplifier current noise and the Rd (11). Dynamic resistance of the array is matched to the noise impedance of the amplifier by proper combination of two CEBs in parallel ($W = 2$) and 64 CEBs in series ($N = 64$).

The total noise is determined mainly by the amplifier noise (JFET) (11) and the *SIN* tunnel junction noise (11). The electron–phonon noise (10) is small due to the small volume of the absorber and the low temperature. As we can see from Figure 7, the noise

performance for the optical power load of 20 fW fits the requirements of $NEP_{tot} < NEP_{phot}$ for $R = 1 \text{ k}\Omega$.

The results of the simulation for the 2D array for different optical power load, P_0 , are shown in Figure 7b. As we can see from Figure 7b, the noise performance for the optical power load $P_0 > 15 \text{ pW}$ fits the requirements of background noise limited performance with $NEP_{tot} < NEP_{phot}$. Relatively large crossover power load is related with a large number of bolometers for wideband realization and consumption of large power load typical for the balloon experiments type of LSPE.

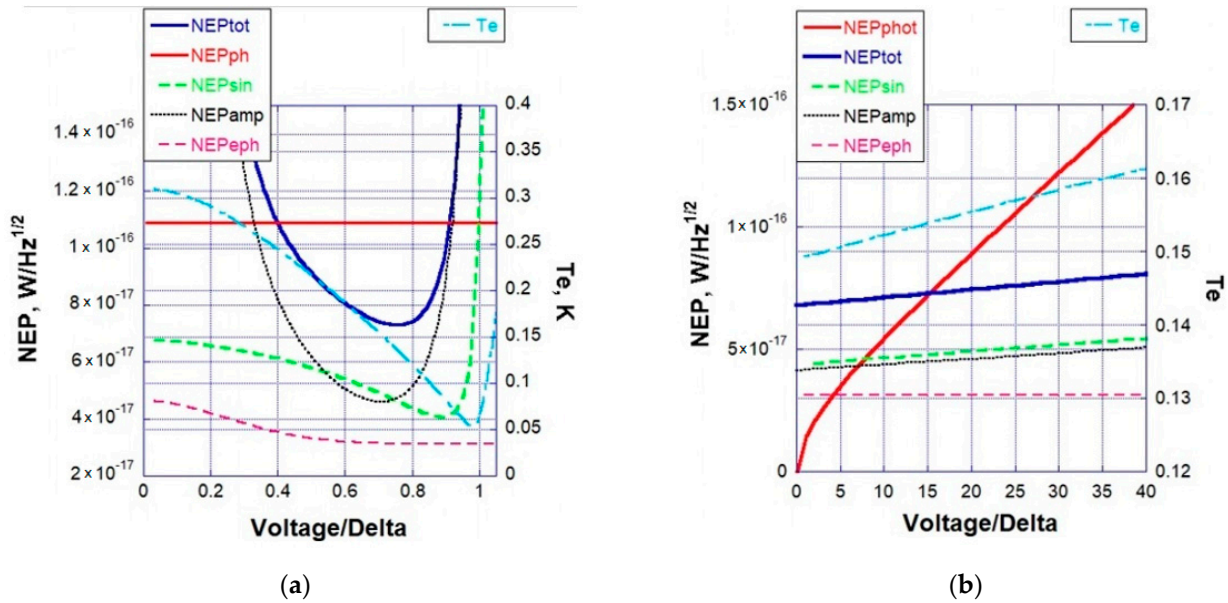


Figure 7. (a) NEP components for the 2D periodic array of cold-electron bolometers with 10×10 unit cells, each containing four bolometers incorporated into a ring. Electron temperature, T_e , is shown for both cases referring to the right axis. Parameters: $f = 350 \text{ GHz}$, $P_0 = 20 \text{ pW}$, $I_{amp} = 5 \text{ fA/Hz}^{1/2}$, $V_{amp} = 5 \text{ nV/Hz}^{1/2}$ (JFET), $R = 1 \text{ k}\Omega$, $\Lambda = 0.02 \text{ }\mu\text{m}^{-3}$, $T = 300 \text{ mK}$, (b) dependence of the noise component and electron temperature on optical power of absorbed signal.

4. Experimental Check

As can be seen in Figure 8, the backward wave oscillator (BWO) acts as a tuneable wave source, whose signal is split by the chopper between the pyroelectric detector and the optical window of the He3 sorption cryostat. The pyroelectric is used as a reference detector for simultaneous calibration of power emission from BWO. Half of the BWO power passes through the chopper and enters the optical window of the cryostat. The window contains a combination of high- and low-pass quasioptical filters and a set of cold neutral density filters which act as cold attenuators to reduce the power of blackbody radiation from the room temperature background. After the filters, the signal is collected by a silicon lens mounted in a holder on the cryostat cold plate. The chip with an array of CEBs is placed on the back of the lens and DC-connected to the room temperature electronics via biasing filters containing cold resistors.

The resulting experimentally measured frequency response [14] normalized to the theoretically expected one is shown in Figure 9. The response decay above 350 GHz is associated with the cut-off frequency of the low-pass quasioptical filter at the cryostat optical window. Experiments with the blackbody radiations source demonstrated the voltage responsivity higher than 10^9 V/W [14].

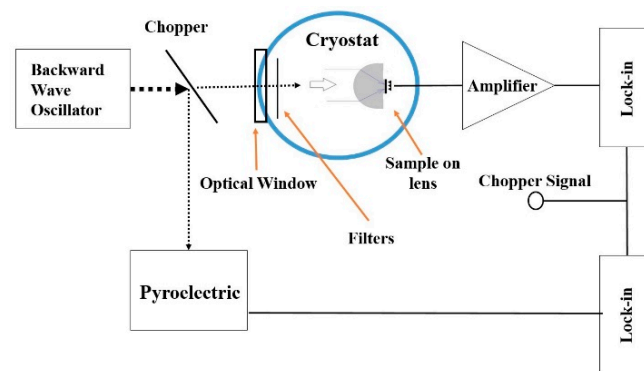


Figure 8. A diagram of the experimental arrangement.

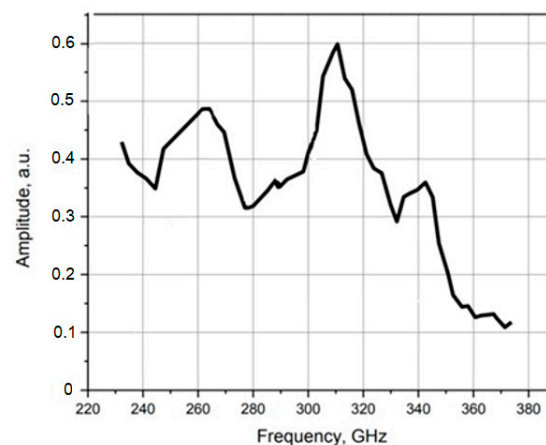


Figure 9. Experimental frequency response of the CEB-array [14].

5. Conclusions

We developed and tested a new concept of the ultra-wideband array of CEBs consisting of sub-wavelength unit cells with voltage responsivity as high as 10^9 V/W and absorbing 80% of the incident power in the frequency range 100–800 GHz. Simulation of the noise performance shows realization of background noise limited performance with $NEP_{tot} < NEP_{phot}$ for the optical power load $P_0 > 15$ pW. We also optimized the structure for performance in two modes, so that we have a high level of the absorption powers for two modes.

Author Contributions: Conceptualization, L.S.K. and A.S.S.; methodology, L.S.K. and A.S.; numerical simulation, B.B.; formal analysis, L.S.K., B.B. and M.Y.L.; writing—original draft preparation, A.S.S., L.S.K. and B.B.; funding acquisition L.S.K. All authors have read and agreed to the published version of the manuscript. All authors have read and agreed to the published version of the manuscript.

Funding: This research was funded by Russian Science Foundation (Project No. 21-79-20227).

Acknowledgments: The authors would like to greatly acknowledge M.A. Tarasov for stimulating discussions and for assistance in samples fabrication and experimental measurements.

Conflicts of Interest: The authors declare no conflict of interest.

References

1. Kuzmin, L.S. Cold-Electron Bolometer. In *BOLOMETERS*; Intechweb.org ed.; Perera, A.G.U., Ed.; Intech: Rijeka, Croatia, 2012; p. 77, ISBN 978-953-510235-9.
2. Tarasov, M.A.; Kuzmin, L.S.; Edel'man, V.S.; Mahashabde, S.; de Bernardis, P. Optical Response of a Cold-Electron Bolometer Array Integrated in a 345-GHz Cross-Slot Antenna. *IEEE Trans. Appl. Supercond.* **2011**, *21*, 3635–3639. [[CrossRef](#)]

3. Kuzmin, L. Ultimate cold-electron bolometer with strong electrothermal feedback. *Proc. SPIE* **2004**, *5498*, 349–361.
4. Kuzmin, L.; Agulo, I.; Fominsky, M.; Savin, A.; Tarasov, M. Optimization of electron cooling by SIN tunnel junctions. *Supercond. Sci. Technol.* **2004**, *17*, s400–s405. [[CrossRef](#)]
5. Gordeeva, A.V. Record electron self-cooling in cold-electron bolometers with a hybrid superconductor-ferromagnetic nanoabsorber and traps. *Sci. Rep.* **2020**, *10*, 21961. [[CrossRef](#)] [[PubMed](#)]
6. Gordeeva, A.V.; Zbrozhek, V.O.; Pankratov, A.L.; Revin, L.S.; Shamporov, V.A.; Gunbina, A.A.; Kuzmin, L.S. Observation of photon noise by cold-electron bolometers. *Appl. Phys. Lett.* **2017**, *110*, 162603. [[CrossRef](#)]
7. Kuzmin, L.S.; Pankratov, A.L.; Gordeeva, A.V.; Zbrozhek, V.O.; Shamporov, V.A.; Revin, L.S.; Blagodatkin, A.V.; Masi, S.; de Bernardis, P. Photon-noise-limited cold-electron bolometer based on strong electron self-cooling for high performance cosmology missions. *Commun. Phys.* **2019**, *2*, 1–8. [[CrossRef](#)]
8. Aiola, S.; Amico, G.; Battaglia, P.; Battistelli, E.; Baù, A.; De Bernardis, P.; Bersanelli, M.; Boscaleri, A.; Cavaliere, F.; Coppolecchia, A.; et al. The Large-Scale Polarization Explorer (LSPE). *Proc. SPIE* **2012**, *8446*, 84467A.
9. Kuzmin, L. 2D Array of Cold-Electron Nanobolometers with Double Polarization Cross-Dipole Antennae. *Nanoscale Res. Lett.* **2012**, *7*, 224. [[CrossRef](#)] [[PubMed](#)]
10. Masi, S.; Ade, P.; Boscaleri, A.; De Bernardis, P.; De Petris, M.; De Troia, G.; Fabry, M.; Iacoangeli, A.; Lamagna, L.; Lange, A.; et al. OLIMPO: A Balloon-Borne, Arcminute-Resolution Survey of the Sky at mm and Sub-mm Wavelengths. In Proceedings of the 16th ESA Symposium on European Rocket and Balloon Programmes and related Research, ESA-SP 530, Sankt Gallen, Switzerland, 2–5 June 2003.
11. Mahashabde, S.; Sobolev, A.; Tarasov, M.; Tsydanzhapov, G.; Kuzmin, L. Planar frequency selective bolometric array at 350 GHz. *IEEE Trans. Terahertz Sci. Technol.* **2015**, *5*, 37–43. [[CrossRef](#)]
12. Mahashabde, S.; Sobolev, A.; Bengtsson, A.; Andren, D.; Tarasov, M.A.; Salatino, M.; De Bernardis, P.; Masi, S.; Kuzmin, L.S. A Frequency Selective Surface Based Focal Plane Receiver for the OLIMPO Balloon-Borne Telescope. *IEEE Trans. Terahertz Sci. Technol.* **2015**, *5*, 145–152. [[CrossRef](#)]
13. Mahashabde, S.; Tarasov, M.A.; Salatino, M.; Sobolev, A.; Masi, S.; Kuzmin, L.S.; de Bernardis, P. A distributed-absorber cold-electron bolometer single pixel at 95 GHz. *Appl. Phys. Lett.* **2015**, *107*, 092602. [[CrossRef](#)]
14. Sobolev, A.S.; Beiranvand, B.; Chekushkin, A.M.; Kudryashov, A.V.; Tarasov, M.A.; Yusupov, R.A.; Gunbina, A.; Vdovin, V.F.; Edelman, V. Wideband metamaterial-based array of SINIS bolometers. *EPJ Web Conf.* **2018**, *195*, 05009. [[CrossRef](#)]
15. Kuzmin, L. Optimization of the Hot-Electron Bolometer for Space Astronomy. In *The International Workshop on Superconducting Nano-Electronics Devices*; Pekola, J., Ruggiero, B., Silvestrini, P., Eds.; Springer: Boston, UK, 2002; pp. 145–154.
16. Golubev, D.; Kuzmin, L. Nonequilibrium theory of a hot-electron bolometer with normal metal-insulator-superconductor tunnel junction. *J. Appl. Phys.* **2001**, *89*, 6464–6472. [[CrossRef](#)]